

**Femtosecond laser induced luminescence in hierarchically structured
Nd³⁺, Yb³⁺, Er³⁺ co-doped upconversion nanoparticles: light-matter interaction
mechanisms from experiments and simulations**

**Guilherme H. Oliveira, Flavia S. Ferreira, Guilherme Ferbonink, Marcos Paulo
Belançon, Fernando A. Sigoli*, René A. Nome***

Institute of Chemistry - State University of Campinas / UNICAMP

Corresponding authors:

* nome@unicamp.br

* fsigoli@unicamp.br

ABSTRACT

Fundamental studies of light-matter interactions are important for basic knowledge and in applications. Thanks to advances in experimental and theoretical methods, nowadays it is possible to perform such studies in a broad dynamic range, covering timescales from that of elementary interactions to real time. In the present work, we perform an experimental-theoretical study of light intensity-dependent femtosecond and CW-laser induced frequency upconversion in hierarchically structured core-multishell nanoparticles co-doped with Nd^{III}, Yb^{III}, and Er^{III}. Upconversion spectra recorded with CW and femtosecond excitation are qualitatively similar whereas the intensity dependence of upconversion depends on excitation mode (CW or femtosecond). To further assess the observed intensity dependence, we perform light-matter interaction simulations in the dynamic range from 100 fs to 3 ms for 18-level system describing the UCNPs, including 9 Nd^{III} levels, 2 Yb^{III}, and 7 Er^{III} levels and a classical model for the excitation source. The calculated time- and intensity-dependent energy level population are compared with measured spectra to understand CW vs femtosecond laser-induced upconversion. To further discuss the differences between CW and femtosecond laser-induced light-matter interactions for the systems studied here, we perform semi-classical pulse propagation simulations and ultrafast pump-probe measurements to study how the light source bandwidth, relative to the absorption linewidth, influence light absorption and transmission and further connect these results with the intensity dependence. Overall, we report our progress toward mechanistic studies of light-matter interaction and photophysical pathways following femtosecond excitation and UCNPs.

INTRODUCTION

Thanks to remarkable advances in theory, computation, and experiments, nowadays it is possible to interrogate a variety of molecular and material processes that cover many orders of magnitude in time. Starting from the earliest fundamental events up to longer times, studies performed at multiple timescales include, for example, glass-transition [1,2], biophysics [3,4] and solar cells [5]. That the examples mentioned span multiple fields of research already speaks for the widespread interest in this growing class of interdisciplinary tools.

Within the field of spectroscopy of lanthanide ions in host matrices and in upconversion nanoparticles (UCNPs), multiple timescales are required to describe all processes in detail, from the basic selection rules to the multitude of energy levels and energy transfer photophysical pathways required to understand the luminescent properties of these materials. This is a challenging task, because the ultrashort laser pulses used to interrogate light-matter interactions at the shortest timescales exhibit high peak intensities. Upon their interaction with UCNPs, ultrashort lasers will thus give rise to both sequential and simultaneous excitation processes, adding complexity to the UCNP photophysics. Moreover, ultrashort laser pulses have broad spectral bandwidth, broader than most of trivalent lanthanide doped-material absorption linewidth, and thus the spectroscopic study must be performed taking this regime into account, thereby adding further complexity to the light-matter interaction study.

Nonetheless, considering the tremendous progress in fundamental understanding of the luminescent properties of lanthanide ions in complexes and host matrices [6-9] as well as UCNPs [10-13], together with the importance of UCNPs in basic science [14,15] and applications [16-18], understanding light-matter interactions involving femtosecond lasers and UCNPs may be useful in studies requiring higher energies, for example, in real-time applications and faster super-resolution bioimaging [19].

Several recent studies have reported fundamental advances in our understanding of energy transfer mechanisms in UCNPs and core-shell UCNPs [20-30]. However, to the best of our knowledge, this work reports for the first time a comparison between experiments and simulations involving femtosecond and CW-induced upconversion with core-triple shell UCNPs containing with Gd^{III} , Nd^{III} , Yb^{III} , and Er^{III} ions. In this work, we describe synthesis and characterization methodologies, experimental setup and simulation details, followed by sample characterization by electron microscopy and intensity-dependent upconversion luminescence. We present kinetic simulation results for a model including Nd^{III} , Yb^{III} , and Er^{III} ions, as well as a realistic model for the femtosecond laser used in this work, as a function of time and excitation intensity, and compare the measured and calculated power-dependent luminescence. We present semi-classical pulse propagation simulations and femtosecond pump-probe measurements for Nd^{III} to help isolate different contributions to the observed UCNP luminescence. We conclude by summarizing the main results reported and discuss possible directions for investigations.

MATERIALS AND METHODS

Materials, synthesis and characterization: All reagents were analytical grade. The syntheses of hierarchically structured upconversion nanoparticles with one core and three shells were performed as described previously [31]. The transmission electron microscopy images were obtained using a Libra 120, (Carl Zeiss) microscope equipped with an omega filter in-column, with LaB6 thermionic emission, operated at 120 kV. An Olympus digital imaging system with Cantega G2 camera (2048 x 2048 pixels / pixel size of 14 μm x 14 μm / 14-bit dynamic range) and iTEM software. The atomic percentages were measured with the TEM-FEG energy dispersive X-ray spectrometer. Briefly, the system consists of core-shell nanoparticles with controlled composition and shape in four distinct regions, as shown schematically in Figure 1. Sample KS4 exhibits core with $\text{NaY}_{0.85}\text{Dy}_{0.15}\text{F}_4$ (gray in Figure 1) composition and three layers with composition NaYF_4 (yellow), $\text{NaGd}_{0.80}\text{Er}_{0.02}\text{Yb}_{0.18}\text{F}_4$ (green), $\text{NaGd}_{0.75}\text{Nd}_{0.25}\text{F}_4$ (red). The AF3 sample has a core with NaDyF_4 composition and three shells with the same composition as sample UCNP KS4. In both samples, the Nd^{III} ion has absorption at 808 nm and the UCNPs exhibit upconversion luminescence. In order to further study light-matter interactions with Nd^{III} alone, experiments and simulations were also performed with low silica calcium aluminosilicate doped with 0.5 % Nd^{III} ions.

Experimental setup: Figure 1 shows schematically the experimental setup used in this work. The setup is a horizontal nonlinear fluorescence microscope consisting of a tunable CW/femtosecond laser (100 fs, 76 MHz), optical isolator, low-pass dichroic mirror, and a sample holder containing UCNP powder samples. Detection was performed in epi-fluorescence geometry by placing the sample holder oriented at normal angle with respect to the incident laser beam and on a three-dimensional micrometer resolution translation stage. Emitted light transmitted through the dichroic was collected with an optical fiber and sent to a spectrograph for upconversion spectral measurements. Before each measurement, the laser is tuned to the excitation wavelength of interest, and we measure the pulse spectrogram for complete characterization of the temporal and spectral profile of the femtosecond laser. During each measurement set, we registered the upconversion spectrum from the UCNP as a function of average laser power, and a portion of the laser power transmitted through the dichroic was sent to a power meter to monitor incident light intensity during the upconversion measurements. The measured emission intensity was steady during the measurement time, thus confirming the photostability of the UCNPs and the absence of drifts or laser heating effects [32]. For each sample, two such sets of measurements were performed, with the laser either in pulsed femtosecond or in continuous wave (CW) operating modes. Ultrafast pump-probe spectroscopy measurements were performed as described previously [33].

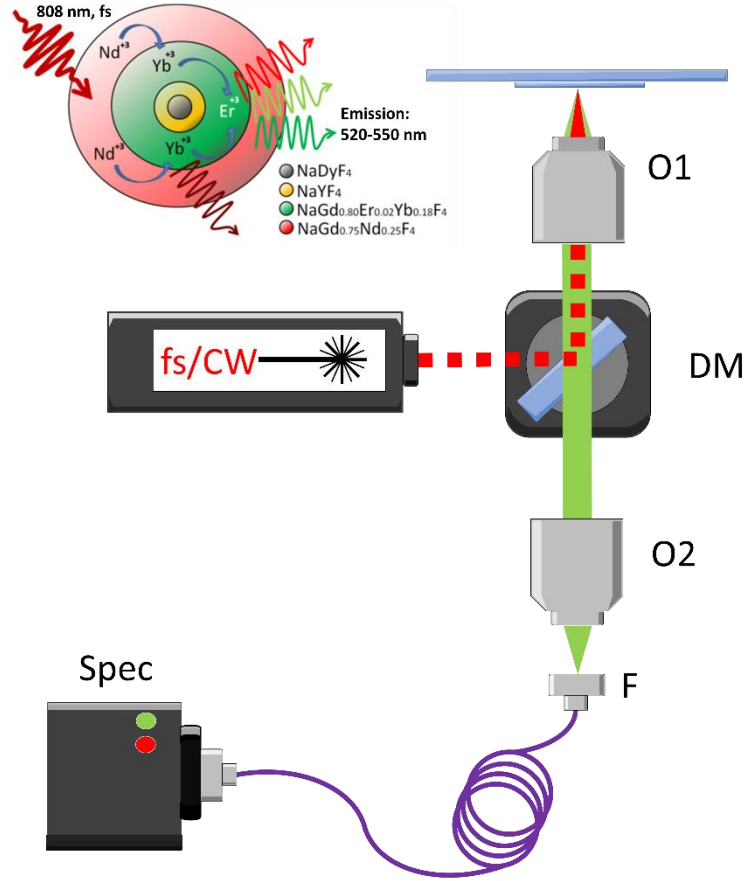
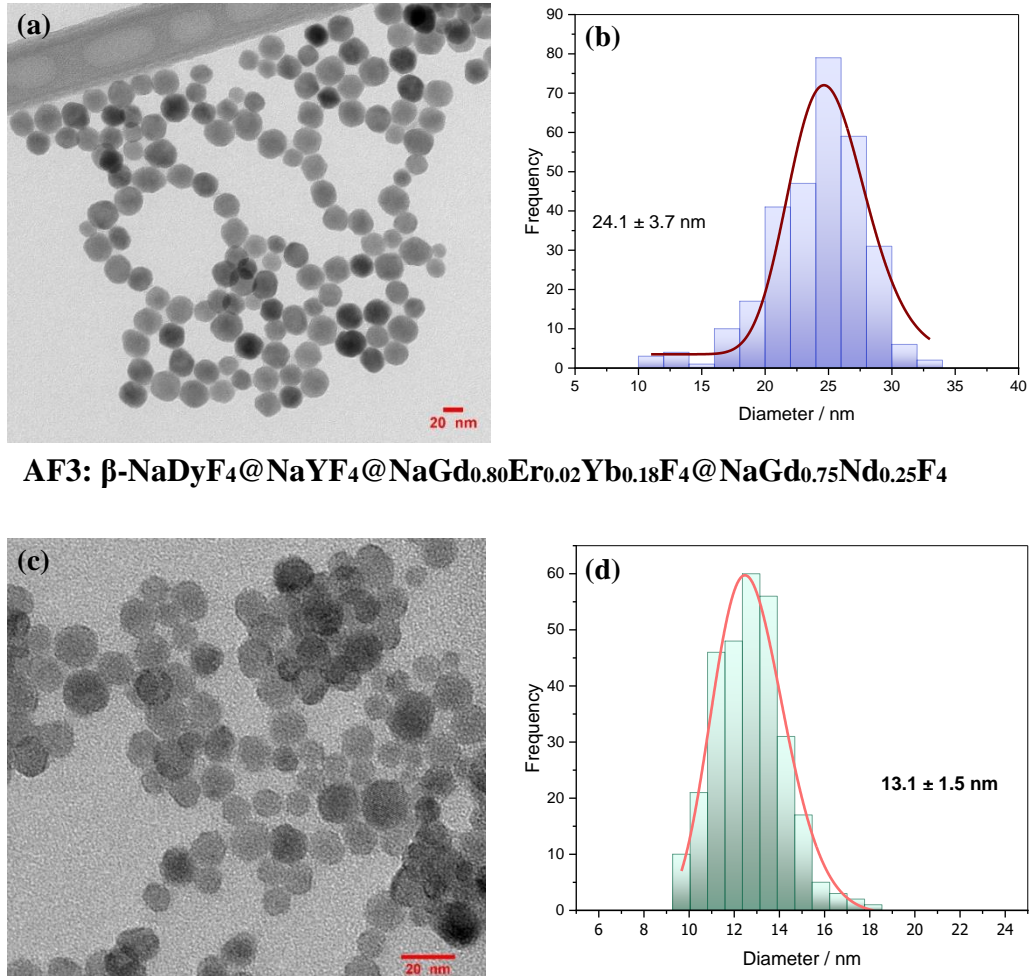


Figure 1. Experimental setup for upconversion measurements. fs/CW: tunable femtosecond/continuous wave excitation; DM: dichroic mirror; O1,O2: objectives; F: optical fiber; Spec: spectrograph. The hierarchical UCNP structures used in the present work are shown schematically.

Simulations: Light-matter interaction in the CW and femtosecond excitation modes were modeled with a semi-classical approach treating light classically and matter with discrete energy diagram. The rate equation approach is similar to numerical studies described previously [34-37], and here we highlight details specific to our implementation. Rate equations for an 18-level system describing Nd^{III}, Yb^{III}, and Er^{III} ions were used to model the population dynamics upon interaction with CW and femtosecond lights. CW excitation was modeled as described previously [33-37], whereas modeling of pulsed femtosecond laser excitation was implemented in the simulations employing a Shah-type function with a 100fs pulse duration (Gaussian function) and 76 MHz repetition rate. Additionally, coupled Maxwell-Schrodinger pulse propagation simulations were employed to study femtosecond laser light interacting with a two-level system absorbing at 808 nm, as in the present experiments [38]. Additional simulation details are given in the Supporting Information.

RESULTS AND DISCUSSION



AF3: β -NaDyF₄@NaYF₄@NaGd_{0.80}Er_{0.02}Yb_{0.18}F₄@NaGd_{0.75}Nd_{0.25}F₄

KS4: NaY_{0.85}Dy_{0.15}F₄@2NaYF₄@2NaGd_{0.80}Er_{0.02}Yb_{0.18}F₄@2NaGd_{0.75}Nd_{0.25}F₄

Figure 2. TEM images and corresponding size distribution histograms of the UCNP samples studied in this work: AF3 (a and b) and KS4 (c and d).

The UCNP samples used in the present work were synthesized and characterized as described previously [31]. Figure 2 shows TEM images and corresponding size distribution histograms of samples AF3 (2a and 2b) and KS4 (2c and 2d). For both samples, the shell doped with Nd^{III} (25%) ions absorbs 808 nm light, and excites Yb^{III} ions migration by interfacial energy transfer (IET) [25], that in its turn transfer the energy to upconverting Er^{III} ions [39]. Therefore, in this core/multi-shell design, the lanthanide-doped upconversion nanoparticles studied here consist of stable dielectric host matrices with low phonon energy with efficient upconversion while minimizing nonradiative relaxation [37,40,41].

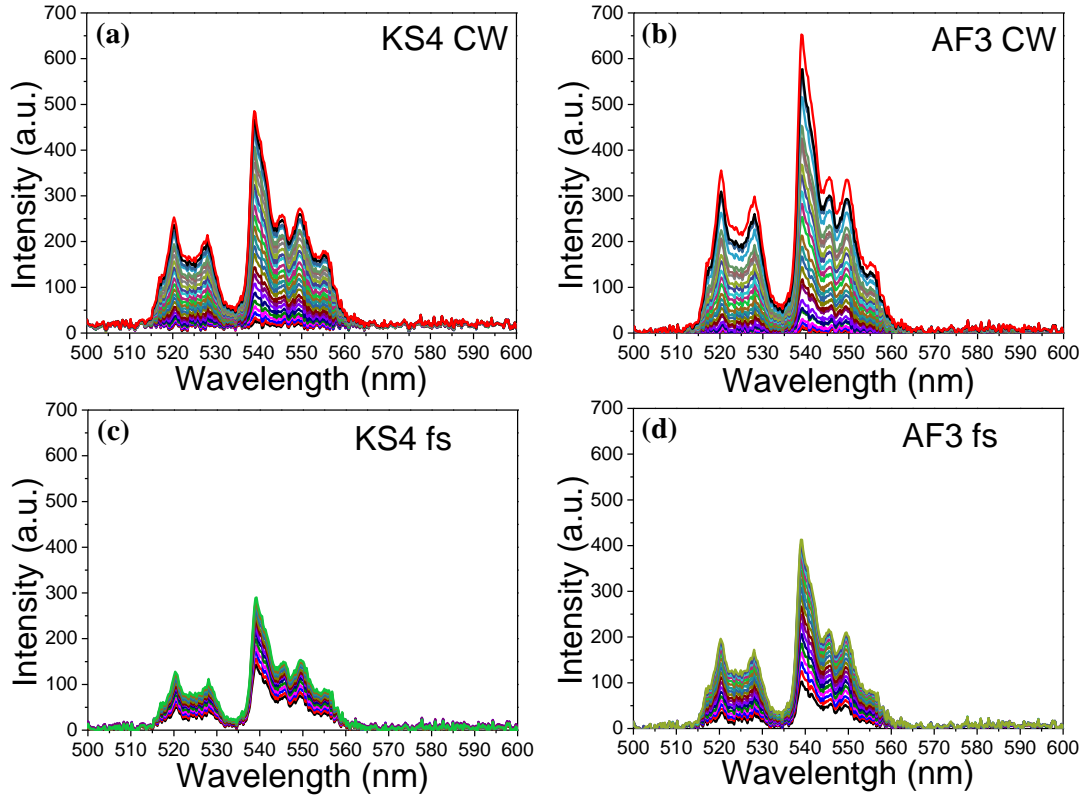


Figure 3. Upconversion luminescence spectra as a function of pump-intensity for samples KS4 (a and c) and AF3 (b and d) excited by CW (top) and femtosecond (bottom) light.

Figure 3 shows the upconversion spectra of KS₄ and AF₃ samples measured using CW (3a and 3b) and femtosecond (3c and 3d) laser excitation, comparing the influence of femtosecond and CW excitation on UCNP luminescence measured with the setup shown in Figure 1. Upconversion luminescence response by femtosecond laser excitation exhibits qualitatively the same spectral response (i.e., bands and peak wavelength values) obtained when the UCNP samples were excited with CW laser. This result shows that the emissive states are the same in both cases, being populated after light absorption followed by excited state relaxation, and thus femtosecond laser-induced excitation can also be used to characterize steady-state upconversion luminescence emission from the UCNP samples studied in this work.

Although the upconversion luminescence spectra measured after excitation is qualitatively similar for CW or femtosecond excitation, their power dependence is different. Figure 4 shows the measured upconversion emission intensities integrated over the bands shown in Figure 3 as function of incident light intensity [32]. In the case of CW excitation (Figure 4a), a nonlinear intensity dependence with upward curvature is observed for both samples. On the other hand, for sample AF₃ upconversion intensity with femtosecond excitation (Figure 4b) leads to a nonlinear excitation intensity dependence as the upconversion emission intensity nears a plateau with increasing power, while for sample KS₄ a nearly linear dependence is observed for sample KS₄.

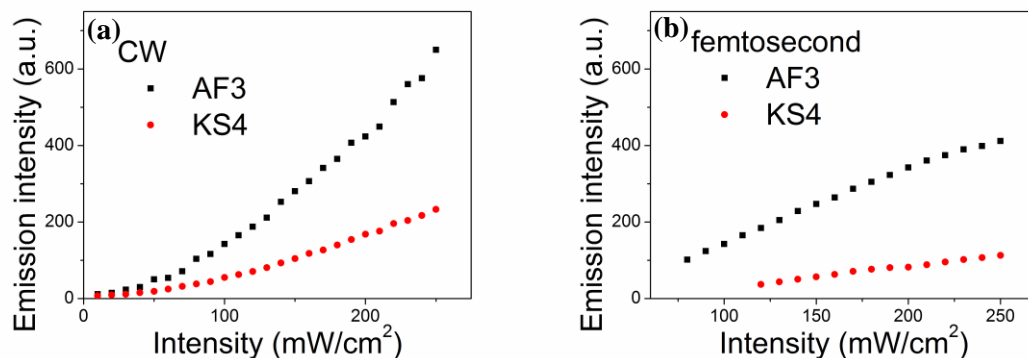


Figure 4. Upconversion luminescence intensities as a function of pump-intensity of samples KS4 (red points) and AF3 (black points) excited by CW(a) and femtosecond (b) light.

As shown in Figures 3 and 4, by varying the incident light intensity and excitation mode (CW or pulsed femtosecond lasers), different regimes of light-matter interaction can be assessed. Due to the high peak power of femtosecond lasers, both sequential and simultaneous resonant excitation mechanisms (with different selection rules for one- and two-photon absorption) may occur, or even coherent non-resonant nonlinearities that employ virtual states, for which upconversion is a second order nonlinear optical process. Therefore, we highlight the different nonlinear optical upconversion processes that can be studied in the regime described with kinetic rate equations and diagrams based on real energy levels that give a nonlinear dependence of luminescence upon excitation light that is not necessarily second order with respect to the incident light electric field.

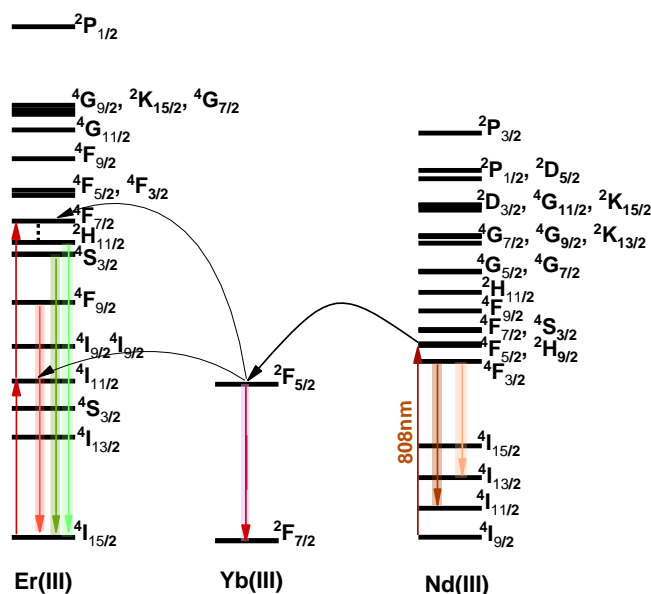


Figure 5. Energy level diagram of the Nd^{III}, Yb^{III}, and Er^{III} ions studied in the simulations. The full set of photophysical pathways considered is included in the Supporting Information.

To model light-matter interactions for the UCNPs shown in Figures 1 and 2, we employ rate equations for an 18-level system to describe energy levels of Nd^{III}, Yb^{III}, and Er^{III} ions, as shown in Figure 5. Photophysical pathways including excited state absorption, energy transfer upconversion, cooperative upconversion, and cross-relaxation, as well as time-dependent excitation intensity are considered (see SI). We employ a nine-level system to describe Nd^{III}, two-level system for Yb^{III} and seven-level system for Er^{III}. The Nd^{III} system includes absorption to $^4F_{5/2}$, relaxation to $^4F_{3/2}$ and energy transfer to Yb^{III} in addition to relaxation channels to lower energies and a dense manifold of higher lying electronic states [33-36]. The Yb^{III} system describes transitions between states $^2F_{7/2}$ and $^2F_{5/2}$. In addition, the $^2F_{5/2}$ level has an additional energy transfer process to electronic energy level of Er^{III}: $^4I_{11/2}$. In the Er^{III} model, we also include additional light-matter interactions describing absorption ($^4I_{15/2} \rightarrow ^4I_{11/2}$ and $^4I_{11/2} \rightarrow ^4F_{7/2}$) and radiative decay: $^2H_{11/2} \rightarrow ^4I_{15/2}$ (520 nm emission), $^4S_{3/2} \rightarrow ^4I_{15/2}$ (550 nm emission) and $^4S_{3/2} \rightarrow ^4F_{9/2}$ (655 nm emission) [12,42]. Additional non-radiative and weaker contributions involving the energy levels shown in Figure 5 are also included in the kinetic model (see SI). The simulation parameters used were taken from earlier models for photophysical processes in Nd^{III}, Yb^{III}, and Er^{III} system [33-36]. We acknowledge that this is still a relatively simple model. More recently, several UCNP photophysical and mechanistic studies [42-46] emphasized the relative importance of specific terms in the kinetic model (or working under specific intensity regimes) that may differ from our implementation. However, given that the main focus of this work is the comparison between experimental and computational CW- and femtosecond-laser induced upconversion, we restrict our study to the effects of power-dependence on population dynamics of the emissive states. Further improvements are certainly needed, as well as comparisons between models, and will be considered in subsequent work. Nonetheless, understanding the light-matter interactions in this simpler case hopefully will provide a basis for further work.

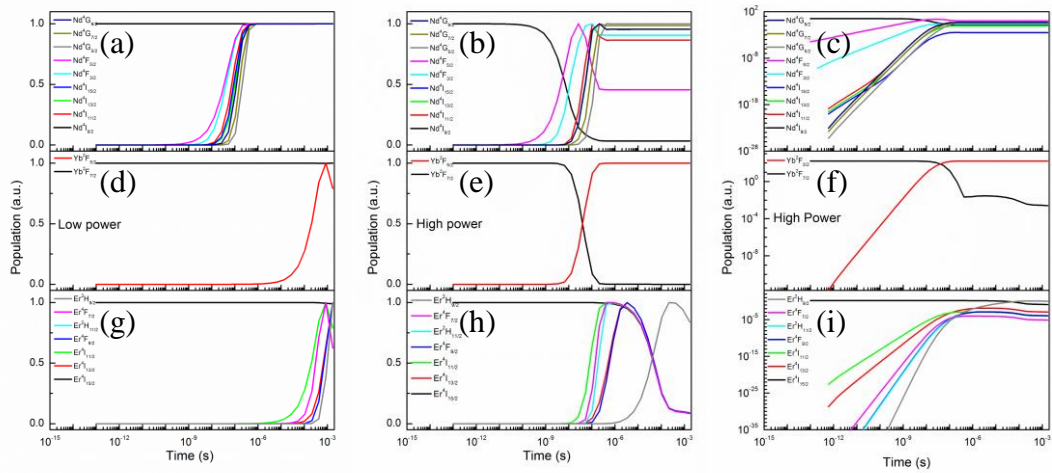


Figure 6. Time-dependent populations for each state in the coupled Nd^{III}-Yb^{III}-Er^{III} system studied in the present work: Nd (top), Yb (center), and Er (bottom). Simulation results are shown for low power (a, d, g), high power on semi-log scale (b, e, h) and high power on log-log scale (c, f, i).

Figure 6 shows the time-dependent normalized populations of each energy level used in the simulations for Nd^{III} (Figures 6a, 6b, and 6c), Yb^{III} (Figures 6d, 6e, and 6f) and Er^{III} (Figures 6g, 6h, and 6i) covering ten orders of magnitude in time, from 100 femtoseconds to 3 milliseconds at low (left column) and high power (center and right power), where in the simulations the photophysical process begins with the Nd^{III} $^4I_{9/2} \rightarrow ^4F_{5/2}$ transition. For Nd^{III} at low power (Fig 6a), initially the population of excited electronic states increases with a sigmoidal pattern, reaching steady state populations at later times, with concomitant decrease in the ground state population of Nd^{III} $^4I_{9/2}$, which is more clearly seen at high power (Fig 6b, 6c).

Upon reaching the steady state for Nd^{III} energy levels, there is an increase in the population of Yb^{III} excited state, $^2F_{5/2}$ (Fig 6d) due to energy transfer Nd^{III} \rightarrow Yb^{III}, with concomitant decrease in Yb^{III} ground state population $^2F_{7/2}$, which is more clearly seen at high power (Fig 6e, 6f). Despite the two sigmoidal-like curves in Figure 6e, we note that there is no population inversion in the Yb^{III} two-level system, as shown in loglog scale in Fig 6f.

Similarly, Yb^{III} \rightarrow Er^{III} energy transfer is observed once Yb^{III} energy levels reach steady state, as indicated by an increase in the population of Er^{III} excited electronic states and decreasing the population of Er^{III} $^4I_{15/2}$ ground state (Fig 6g). Therefore, in going from Fig 6a to 6d to 6g, the time-dependent populations show an overall mechanism of energy transfer from Nd^{III} to Yb^{III} and then Er^{III}, consistent with the energy-level diagram shown in Figure 5 and with the UCNP's studied in this work (Figures 1 and 2).

In going from low power to high power, the overall trend discussed above is observed as well. However, at high power (Figs 6b, 6e, and 6h), the overall population kinetics shifts so that state-to-state transitions are observed at earlier times. Additionally, at high power individual electronic states exhibit peaked time-dependent probabilities that also allow identification of specific electronic states (for example, see the curves for Nd^{III} $^4F_{5/2}$ in Fig 6b and for Er^{III} $^4F_{7/2}$ in Fig 6h). Figs 6c, 6f, and 6i show the same simulation results at high power, except that a loglog scale is used, showing that population of excited electronic states increases even at the shortest times.

We repeated the calculations described above for a range of input pump intensities and plot the population of emissive states as a function of pump intensity. Figure 7(top row) shows a linear plot of steady-state population (which is proportional to fluorescence intensity) of Er^{III} $^2H_{11/2}$ electronic state as a function of pump intensity, which allows us to study the linear and nonlinear regimes of intensity dependence in upconversion.

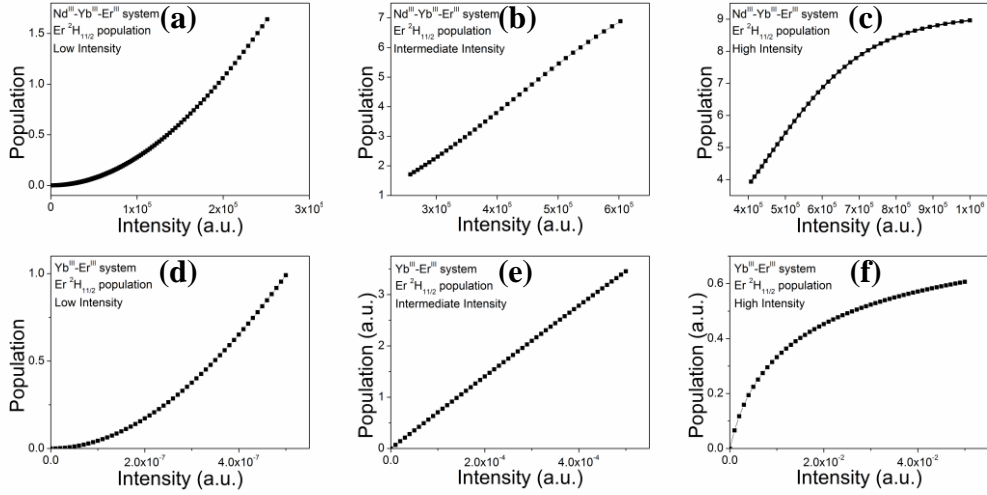


Figure 7. Linear plot of $\text{Er}^{\text{III}} 2\text{H}_{11/2}$ population as a function of incident femtosecond pulsed light intensity for $\text{Nd}^{\text{III}}\text{-Yb}^{\text{III}}\text{-Er}^{\text{III}}$ (top row) and $\text{Yb}^{\text{III}}\text{-Er}^{\text{III}}$ (bottom row): low power, (a) and (d); intermediate power, (b) and (e); high power (c) and (f).

As shown in Figure 7(top row), a nonlinear intensity dependence is observed at low (Figure 7a) and high (Figure 7c) power, with upward and downward curvatures, respectively. On the other hand, a linear intensity dependence is observed at intermediate pump power (Figure 7b). Specifically, at low power, the population increases nonlinearly as approximately the second power of incident light intensity (Figure 7a). At intermediate power, an approximately linear relation is observed for the population as a function of incident power (Figure 7b). At high intensity, a slope less than one is observed, and the system tends to saturation of population of energy level $\text{Er}^{\text{III}} 2\text{H}_{11/2}$ (Figure 7c) [41,42,47]. We also performed simulations for $\text{Yb}^{\text{III}}\text{-Er}^{\text{III}}$ system (without Nd^{III} and exciting the $\text{Yb}^{\text{III}} 2\text{F}_{7/2} \rightarrow 2\text{F}_{5/2}$ transition), and the results are shown in Figure 7 (bottom row). Clearly, the nonlinear intensity dependence is observed for both $\text{Nd}^{\text{III}}\text{-Yb}^{\text{III}}\text{-Er}^{\text{III}}$ and $\text{Yb}^{\text{III}}\text{-Er}^{\text{III}}$ systems, which is helpful for understanding the mechanism of energy transfer.

In comparing experimental and simulated results, we observe that the trends observed experimentally (Figures 3 and 4) can be described from the light-matter interactions summarized in Figure 5. Specifically, upconversion spectra measured using CW excitation (Figures 3a and 3b) fall within the low power regime observed in the simulations (Figure 7a). On the other hand, experimental results obtained using femtosecond light excitation (Figures 3c and 3d) can be described with the intermediate and high power regimes observed in the simulations (Figures 7b and 7c). Even though the same nominal power (measured with a power meter) was used in the upconversion measurements performed with CW and femtosecond laser, excitation from 100 fs pulses leads to several orders of magnitude higher peak intensities and instantaneous nonlinearities. In this way, we can describe the trends observed experimentally in terms of nonlinear, intensity-dependent light-matter interactions in the $\text{Nd}\text{-Yb-Er}$ system. Additional work is needed to describe in more detail the results observed experimentally, and thus to apply the methodology to other systems as well [48]. For example, although

an upward curvature is observed in both experiments and simulations at low power with an order approximately equal to two, the specific polynomial order is dependent upon radiative/non-radiative rate constants, which should be informed by time-resolved spectroscopic measurements.

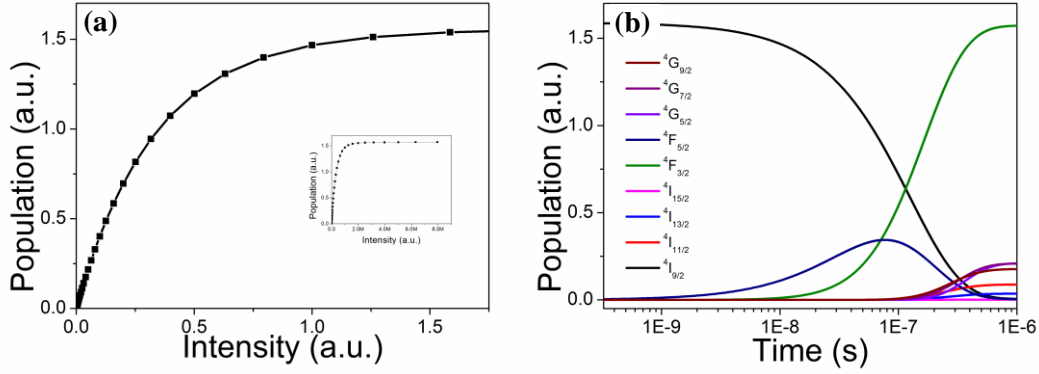


Figure 8. (a) Linear plot of Nd^{III} $4F_{3/2}$ energy level population as a function of incident power intensity. (b) Nd^{III} population as a function of time for the highest intensity studied in this work. The population of Nd^{III} energy levels $4I_{11/2}$, $4I_{13/2}$, $4I_{15/2}$, $4G_{5/2}$, $4G_{7/2}$ and $2G(1)_{9/2}$ have been multiplied by a factor of 100 to aid visualization.

The comparison between experiments and simulations discussed above focused on emission from a specific electronic state, namely, Er^{III} $2H_{11/2}$. Similar intensity dependence (that is, a saturation-type curve) is observed by studying other Er^{III} emissive electronic states, for example, Er^{III} $4F_{9/2}$ and $4S_{3/2}$. In addition to the Nd^{III} - Yb^{III} - Er^{III} and Yb^{III} - Er^{III} systems, we have performed simulations for just one subsystem, Nd^{III} including the nine-energy levels shown in Figure 5. Figure 8a shows a linear plot of the population of Nd^{III} $4F_{3/2}$ state as a function of pump intensity for this subsystem. A saturation-type curve is observed for the population of Nd^{III} $4F_{3/2}$ state with increasing pump intensity, reaching a plateau in the population at higher intensities. Figure 8b shows the time-dependent populations of all nine Nd^{III} electronic states at the highest pump intensity studied in the simulations. The highest populations are observed for states $4I_{9/2}$, $4F_{5/2}$ and $4F_{3/2}$ as the system evolves in time from $4I_{9/2}$ (ground state) to $4F_{5/2}$ (intermediate state) to $4F_{3/2}$ (steady-state), while other states are populated to a lesser degree. Overall, the results shown in Figure 8 also illustrate how light intensity influences the time-dependent and steady-state populations in the systems studied in this work.

Given that lanthanide ions exhibit absorption lineshapes narrower than the femtosecond laser bandwidth, light-matter interactions will also depend on the linewidth of the excitation source [38]. For example, we have performed resonant pulse propagation simulations through an ensemble of two-level systems combining Maxwell's equations to model pulse propagation and Schrodinger equation for the two-level system and a Kubo model for the material lineshape. The simulation parameters for the two-level system are modeled after experimental parameters for Nd^{III} absorption at 808 nm excitation with a

constant value for the material linewidth. The parameters for the light source are such that the pulses are resonant with the two-level system and with tunable laser bandwidth.

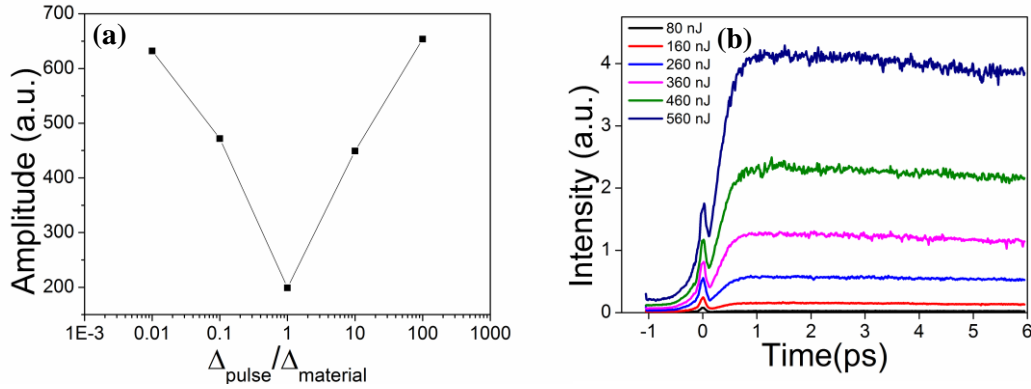


Figure 9. (a) Finite-difference time-domain semi-classical simulations of pulse amplitude as a function of the ratio between pulse bandwidth to material absorption linewidth for a two-level system. (b) Ultrafast pump-probe measurements as a function of time and pump energy for low silica calcium aluminosilicate doped with 0.5 % Nd^{III} ions.

Figure 9 (a) shows simulation results of pulse amplitude after propagating through the sample as a function of the ratio between pulse linewidth and material linewidth. In the range where $\Delta_{\text{pulse}}/\Delta_{\text{material}} \leq 1$, the pulse amplitude after the sample decreases with increasing pulse linewidth, due to stronger light absorption, reaching a saturation limit where $\Delta_{\text{pulse}}/\Delta_{\text{material}} = 1$. In contrast, in the range where $\Delta_{\text{pulse}}/\Delta_{\text{material}} \geq 1$, the pulse amplitude after the sample increases with increasing pulse linewidth, due to pulse content at the spectral wings that is off-resonant with respect to the material linewidth. This regime also gives rise to beats in the propagated pulse due to interaction between the macroscopic polarization and the incident light during the timescale of the material dephasing time, as described previously for other systems [38]. Thus, depending on the pulse linewidth relative to the material linewidth, different light-matter interactions regimes are observed, which affects the effective intensity absorbed.

In order to further illustrate the differences between CW and femtosecond laser induced light-matter interactions for materials containing lanthanide ions, we have performed ultrafast pump-probe measurements as a function of pump intensity for a sample consisting a low silica calcium aluminosilicate doped with 0.5 % Nd^{III} ions. The measurements are performed with femtosecond laser pulses that are resonant with the sample and linewidth broader than the material linewidth. Figure 9(b) shows the results of pump-probe signal as a function of time delay for pulse energies ranging from 80 nJ to 560 nJ. At all intensities studied, the signal at time zero corresponds to the instantaneous electronic nonlinearity, followed by a slowly decaying signal that increases in amplitude with increasing pump intensity. The time profile is associated with a beat in the excited state population in the light-matter interaction regime studied in this work, leading to a transient destructive interference between macroscopic nonlinear polarization and the

incident pulse on timescales shorter than the sample intrinsic dephasing time. At longer time delay, this is followed by an increase transient transmission of the probe pulse with longtime scale decay time (population time) for the excited electronic state.

CONCLUSIONS

In conclusion, we have measured upconversion spectra as a function of pump power for hierarchically structured UCNPs excited by CW and femtosecond laser pulses. For both samples, a nearly quadratic pump-power dependence was observed under CW excitation, consistent with low-energy density excitation regime. On the other hand, for femtosecond pulse excitation, linear and sublinear pump-dependence was observed, consistent with high-energy density excitation regime. Numerical modeling of kinetic rate equations for a 18-level system including Nd^{III} (9 levels), Yb^{III} (2 levels) and Er^{III} (7 levels) together with a pulsed light source modeling of femtosecond excitation was used to study the time- and intensity-dependent populations. The analysis is consistent with a net energy flow from Nd^{III} to Yb^{III} and then to the Er^{III} emissive states. Additionally, the overall dynamics is faster with increasing pump power. Intensity dependence of the Er^{III} green emissive state is qualitatively consistent with the experimental results, thus showing how the simulations help resolve the different pump-power dependencies observed upon CW and femtosecond laser excitation with the same nominal power. By looking at the Nd^{III} electronic states time- and intensity-dependence, we observe already at this light-matter interaction process a saturation behavior at the highest power, while also highlighting the importance of two electronic states of Nd^{III} in describing the overall pump dependence. Maxwell-Schrodinger simulations of pulse propagation in resonance with a two-level system modeled after the optical excitation Nd^{III} were performed as a function of laser bandwidth relative to the material linewidth. These simulations were consistent with results from femtosecond pump-probe measurements of model glass host matrix doped with Nd^{III}. Overall, the set of results and simulations presented here help understand the nature of light-matter interactions involving femtosecond lasers and lanthanide ions in upconversion nanoparticles. Further work is needed to enable the study of other UCNPs systems and their mechanistic photophysical dynamics. For example, we plan to extend the model more realistic energy level diagrams, study concentration dependence, include spatial discretization of the sample to discuss distance-dependence of pump-intensity-dependent energy transfer, orientation-dependence of energy transfer, and extension to include nonlinear optical susceptibilities to assess the relative importance of distinct nonlinear optical upconversion mechanisms.

ACKNOWLEDGEMENTS

Financial support from FAPESP (grant 13/22127-2, 14/50906-9, 16/23430-9) and CNPq (the National Council for Scientific and Technological Development) INCT Catalysis in Molecular and Nanostructured Systems is gratefully acknowledged.

REFERENCES

- [1] T. Hecksher, D.H. Torchinsky, C. Klieber, J.A. Johnson, J.C. Dyre, K.A. Nelson, *Proc. Nat. Acad. Sci. USA* 114 (2017) 8710.
- [2] S. Karmakar, C. Dasgupta, S. Sastry, *Annu. Rev. Condens. Matter Phys.* 5 (2014) 255.
- [3] H.S. Chung, W.A. Eaton. *Curr. Opin. Struct. Biol.* 48 (2018) 30.
- [4] D. Sardana, K. Yadav, H. Shweta, N.S. Clovis, P. Alam, S. Sen, *J. Phys. Chem. B* 123 (2019) 10202.
- [5] K.S. Wilson, C.Y. Wong, *J. Phys. Chem. A* 122 (2018) 6438.
- [6] A.N.C. Neto, R.T. Moura Jr, O.L. Malta, *J. Lumin.* 210 (2019) 342.
- [7] M. Seshadri, L.C. Barbosa, C.M.B. Cordeiro, M. Radha, F.A. Sigoli, Y.C. Ratnakaram, *J. Lumin.* 166 (2015) 8.
- [8] J.H.S.K. Monteiro, A. Bettencourt-Dias, F.A. Sigoli, *Inorg. Chem.* 56 (2017) 709.
- [9] A.N.C. Neto, R.T. Moura Jr, A. Shyichuk, V. Paterlini, F. Piccinelli, M. Bettinelli, O.L. Malta, *J. Phys. Chem. C*, 124 (2020) 10105.
- [10] J.F. Suyver, J. Grimm, K.W. Kramer, H.U. Gudel, *J. Lumin.* 114 (2005) 53.
- [11] O. Lehmann, K. Kompe, M. Haase, *J. Am. Chem. Soc.* 126 (2004) 14935.
- [12] G. Liu, *Chem. Soc. Rev.* 44 (2015) 1635.
- [13] L. Tu, X. Liu, F. Wu, H. Zhang, *Chem. Soc. Rev.* 44 (2015) 1331.
- [14] D. Jin, P. Xi, B. Wang, L. Zhang, J. Enderlein, A.M. van Oijen, *Nat. Methods* 15 (2018) 415.
- [15] R.A. Nome, C. Sorbello, M. Jobbágy, B.C. Barja, V. Sanches, J.S. Cruz, V.F. Aguiar, *Meth. Appl. Fluoresc.* 5 (2017) 014005.
- [16] Z. Nie, X. Ke, D. Li, Y. Zhao, L. Zhu, R. Qiao, X.L. Zhang, *J. Phys. Chem. C*, 123 (2019) 22959.
- [17] P.C. Sousa Filho, J. Alain, G. Lemenager, E. Larquet, J. Fick, O.A. Serra, T. Gacoin, *J. Phys. Chem. C* 123 (2019) 2441.
- [18] S.H. Nam, Y.M. Bae, Y.I. Park, J.H. Kim, H.M. Kin, J.S. Choi, K.T. Lee, T. Hyeon, Y.D. Suh, *Angew. Chem.* 123 (2011) 6217.
- [19] R. Diekmann, M. Kahnwald, A. Schoenit, J. Derschamps, U. Matti, J. Ries, *Nature Meth.* 17 (2020) 909.
- [20] J. Kong, X. Shang, W. Zheng, X. Chen, D. Tu, M. Wang, J. Song, J. Qu, *J. Phys. Chem. Lett.* 11 (2020) 3672.
- [21] F. Rabbouw, P.T. Prins, P. Villanueva-Delgado, M. Castelijns, R.G. Geitenbeek, A. Meijerink, *ACS Nano* 12 (2018) 4812.
- [22] F. Wang, R. Deng, J. Wang, Q. Wang, Y. Han, H. Zhu, X. Chen, X. Liu, *Nat. Mater.* 10 (2011) 968.
- [23] X. Huang, J. Lin, *J. Mater. Chem. C* 3 (2015) 7652.
- [24] W. Zhang, J. Li, H. Lei, B. Li, *Opt. Exp.* 28 (2020) 12450.
- [25] B. Zhou, L. Tao, Y. Chai, S.P. Lau, Q. Zhang, Y.H. Tsang, *Angew. Chemie - Int. Ed.* 55 (2016) 12356.
- [26] A.S. Sousa, L.A.O. Nunes, I.G.N. Silva, F.A.M. Oliveira, L.L. da Luz, H.F. Brito, M.C.F.C. Felinto, R.A.S. Ferreira, S.A. Júnior, L.D. Carlos, O.L. Malta, *Nanoscale* 8 (2016) 5327.
- [27] C. Sorbello, P. Gross, C.A. Strassert, M. Jobbagy, B.C. Barja, *ChemPhysChem* 18 (2017) 1407.

- [28] T. Jung, H.L. Jo, S.H. Nam, B. Yoo, Y. Cho, J. Kim, H. Min, Kim, T. Hyeon, Y.D. Suh, H. Lee, K. T. Lee, *Phys. Chem. Chem. Phys.* 17 (2015) 13201.
- [29] L. Liang, D.B.L. Teh, N.-D. Dinh, W. Chen, Q. Chen, Y. Wu, S. Chowdhury, A. Yamanaka, T.C. Sum, C.-H. Chen, N.V. Thakor, A.H. All, X. Liu, *Nat. Commun.* 10 (2019) 1391.
- [30] E. Lee, M. Jung, Y. Han, G. Lee, K. Shin, H. Lee, K.T. Lee, *J. Phys. Chem. C* 121 (2017) 21073.
- [31] E.M. Rodrigues, D.A. Gállico, M.A. Lemes, J. Bettini, I.O. Mazali, M. Murugesu, F.A. Sigoli, *New J. Chem.* 42 (2018) 13393.
- [32] R.E. Joseph, C. Jiménez, D. Hudry, G. Gao, D. Busko, D. Biner, A. Turshatov, K. Krämer, B.S. Richards, I.A. Howard, *J. Phys. Chem. A* 123 (2019) 6799.
- [33] G.F. Ferbonink, T.S. Rodrigues, D.P. dos Santos, P.H.C. Camargo, R.Q. Albuquerque, R.A. Nome, *Faraday Discuss.* 208 (2018) 269.
- [34] M. Pollnau, P.J. Hardman, W.A. Clarkson, D.C. Hanna, *Opt. Commun.* 147 (1998) 203.
- [35] B.-C. Hwang, S. Jiang, T. Luo, J. Watson, G. Sorbello, N. Peyghambarian, *J. Opt. Soc. Am. B* 17 (2000) 833.
- [36] Y. Hu, S. Jiang, G. Sorbello, T. Luo, Y. Ding, B.-C. Hwang, J.-H. Kim, H.-J. Seo, N. Peyghambarian, *J. Opt. Soc. Am. B* 18 (2000) 1928.
- [37] M.Y. Hossan, A. Hor, Q.A. Luu, S.J. Smith, P.S. May, M.T. Berry, *J. Phys. Chem. C* 121 (2017) 16592.
- [38] J.A. Gruetzmacher, R.A. Nome, A.M. Moran, N.F. Scherer, *J. Chem. Phys.* 129 (2008) 224502.
- [39] T. Wang, H. Zhou, Z. Yu, G. Zhou, J. Zhou, D. Huang, L. Sun, P. Gao, Y. Sun, J. Hu, *J. Phys. Chem. C* 122 (2018) 10113.
- [40] K. Shin, T. Jung, E. Lee, G. Lee, Y. Goh, J. Heo, M. Jung, E.-J. Jo, H. Lee, M.-G. Kim, K.T. Lee, *Phys. Chem. Chem. Phys.* 19 (2017) 9739.
- [41] T.A. Laurence, Y. Liu, M. Zhang, M.J. Owen, J. Han, L. Sun, C. Yan, and G.-Y. Liu, *J. Phys. Chem. C* 2018, 122 (2018) 23780.
- [42] R.B. Anderson, S.J. Smith, P. S. May, M.T. Berry, *J. Phys. Chem. Lett.* 5 (2014) 36.
- [43] J. Kong, X. Shang, W. Zheng, X. Chen, D. Tu, M. Wang, J. Song, J. Qu, *J. Phys. Chem. Lett.* 11 (2020) 3672.
- [44] M. Xue, X. Zhu, X. Qiu, Y. Gu, W. Feng, F. Li, *ACS Appl. Mat. Int.* 8 (2016) 17894.
- [45] X. Huang, *Opt. Lett.* 40 (2015) 3599.
- [46] Y.-F. Wang, G.-Y. Liu, L.-D. Sun, J.-W. Xiao, J.-C. Zhou, C.-H. Yan, *ACS Nano* 7 (2013) 7200.
- [47] Z. Li, Y. Zhang, S. Jiang, *Adv. Mater.* 20 (2008) 4765.
- [48] C. Homann, L. Krukewitt, F. Frenzel, B. Grauel, C. Würth, U. Resch-Genger, M. Haase, *Angew. Chem. Int. Ed.* 57 (2018) 8765.

SUPPORTING INFORMATION

Femtosecond laser induced luminescence in hierarchically structured Nd³⁺, Yb³⁺, Er³⁺ co-doped upconversion nanoparticles: light-matter interaction mechanisms from experiments and simulations

Guilherme H. Oliveira, Flavia S. Ferreira, Guilherme Ferbonink, Marcos Paulo
Belançon, Fernando A. Sigoli*, René A. Nome*

Corresponding authors:

* nome@unicamp.br

* fsigoli@unicamp.br

RATE EQUATION SIMULATIONS

$$\begin{aligned}\frac{d n_{Nd^{III} \ ^2G_{9/2}}}{dt} &= W3 \left(n_{Nd^{III} \ ^4F_{3/2}} \right)^2 - \frac{n_{Nd^{III} \ ^2G_{9/2}}}{\tau_{Nd^{III} \ ^2G_{9/2}}} \\ \frac{d n_{Nd^{III} \ ^4G_{7/2}}}{dt} &= W2 \left(n_{Nd^{III} \ ^4F_{3/2}} \right)^2 + \frac{n_{Nd^{III} \ ^2G_{9/2}}}{\tau_{Nd^{III} \ ^2G_{9/2}}} - \frac{n_{Nd^{III} \ ^4G_{7/2}}}{\tau_{Nd^{III} \ ^4G_{7/2}}} \\ \frac{d n_{Nd^{III} \ ^4G_{5/2}}}{dt} &= W1 \left(n_{Nd^{III} \ ^4F_{3/2}} \right)^2 + \frac{n_{Nd^{III} \ ^4G_{7/2}}}{\tau_{Nd^{III} \ ^4G_{7/2}}} - \frac{n_{Nd^{III} \ ^4G_{5/2}}}{\tau_{Nd^{III} \ ^4G_{5/2}}} \\ \frac{d n_{Nd^{III} \ ^4F_{5/2}}}{dt} &= I(t) n_{Nd^{III} \ ^4I_{9/2}} + \frac{n_{Nd^{III} \ ^4G_{5/2}}}{\tau_{Nd^{III} \ ^4G_{5/2}}} - \frac{n_{Nd^{III} \ ^4F_{5/2}}}{\tau_{Nd^{III} \ ^4F_{5/2}}} \\ \frac{d n_{Nd^{III} \ ^4F_{3/2}}}{dt} &= \frac{n_{Nd^{III} \ ^4F_{5/2}}}{\tau_{Nd^{III} \ ^4F_{5/2}}} - \frac{n_{Nd^{III} \ ^4F_{3/2}}}{\tau_{Nd^{III} \ ^4F_{3/2}}} \\ &\quad - 2(W1 + W2 + W3) \left(n_{Nd^{III} \ ^4F_{3/2}} \right)^2 - W_{DNdAYb} n_{Nd^{III} \ ^4F_{3/2}} n_{Yb^{III} \ ^2F_{7/2}} \\ \frac{d n_{Nd^{III} \ ^4I_{15/2}}}{dt} &= \beta_{43} \frac{n_{Nd^{III} \ ^4F_{3/2}}}{\tau_{Nd^{III} \ ^4F_{3/2}}} + \frac{n_{Nd^{III} \ ^4I_{15/2}}}{\tau_{Nd^{III} \ ^4I_{15/2}}} - \frac{n_{Nd^{III} \ ^4I_{13/2}}}{\tau_{Nd^{III} \ ^4I_{13/2}}} + W2 \left(n_{Nd^{III} \ ^4F_{3/2}} \right)^2 \\ \frac{d n_{Nd^{III} \ ^4I_{11/2}}}{dt} &= \beta_{41} \frac{n_{Nd^{III} \ ^4F_{3/2}}}{\tau_{Nd^{III} \ ^4F_{3/2}}} + \frac{n_{Nd^{III} \ ^4I_{13/2}}}{\tau_{Nd^{III} \ ^4I_{13/2}}} - \frac{n_{Nd^{III} \ ^4I_{11/2}}}{\tau_{Nd^{III} \ ^4I_{11/2}}} + W3 \left(n_{Nd^{III} \ ^4F_{3/2}} \right)^2 \\ \frac{d n_{Nd^{III} \ ^4I_{9/2}}}{dt} &= -R05 n_{Nd^{III} \ ^4I_{9/2}} + \beta_{40} \frac{n_{Nd^{III} \ ^4F_{3/2}}}{\tau_{Nd^{III} \ ^4F_{3/2}}} \\ &\quad + \frac{n_{Nd^{III} \ ^4I_{11/2}}}{\tau_{Nd^{III} \ ^4I_{11/2}}} + W_{DNdAYb} n_{Nd^{III} \ ^4F_{3/2}} n_{Yb^{III} \ ^2F_{7/2}}\end{aligned}$$

$$\begin{aligned}
\frac{d n_{Yb^{III} \ ^2F_{5/2}}}{dt} &= W_{DNdAYb} n_{Nd^{III} \ ^4F_{3/2}} n_{Yb^{III} \ ^2F_{7/2}} - W_{DYb^{III} \ ^2F_{5/2} - AEr^{III} \ ^4I_{11/2}} n_{Yb^{III} \ ^2F_{5/2}} n_{Er^{III} \ ^4I_{15/2}} \\
&- W_{DYb^{III} \ ^2F_{5/2} - AEr^{III} \ ^4F_{9/2}} n_{Yb^{III} \ ^2F_{5/2}} n_{Er^{III} \ ^4I_{13/2}} - W_{DYb^{III} \ ^2F_{5/2} - AEr^{III} \ ^4F_{7/2}} n_{Yb^{III} \ ^2F_{5/2}} n_{Er^{III} \ ^4I_{11/2}} \\
&- W_{DYb^{III} \ ^2F_{5/2} - AEr^{III} \ ^2H_{9/2}} n_{Yb^{III} \ ^2F_{5/2}} n_{Er^{III} \ ^4F_{9/2}} \\
\frac{d n_{Yb^{III} \ ^2F_{7/2}}}{dt} &= -W_{DNd - AYb} n_{Nd^{III} \ ^4F_{3/2}} n_{Yb^{III} \ ^2F_{7/2}} + W_{DYb^{III} \ ^2F_{5/2} - AEr^{III} \ ^4I_{11/2}} n_{Yb^{III} \ ^2F_{5/2}} n_{Er^{III} \ ^4I_{15/2}} \\
&+ W_{DYb^{III} \ ^2F_{5/2} - AEr^{III} \ ^4F_{9/2}} n_{Yb^{III} \ ^2F_{5/2}} n_{Er^{III} \ ^4I_{13/2}} + W_{DYb^{III} \ ^2F_{5/2} - AEr^{III} \ ^4F_{7/2}} n_{Yb^{III} \ ^2F_{5/2}} n_{Er^{III} \ ^4I_{11/2}} \\
&+ W_{DYb^{III} \ ^2F_{5/2} - AEr^{III} \ ^2H_{9/2}} n_{Yb^{III} \ ^2F_{5/2}} n_{Er^{III} \ ^4F_{9/2}} \\
\frac{d n_{Er^{III} \ ^2H_{9/2}}}{dt} &= W_{DYb^{III} \ ^2F_{5/2} - AEr^{III} \ ^2H_{9/2}} n_{Yb^{III} \ ^2F_{5/2}} n_{Er^{III} \ ^4F_{9/2}} - \frac{n_{Er^{III} \ ^2H_{9/2}}}{\tau_{r,Er^{III} \ ^2H_{9/2} \rightarrow Er^{III} \ ^4I_{15/2}}} \\
\frac{d n_{Er^{III} \ ^4F_{7/2}}}{dt} &= W_{DYb^{III} \ ^2F_{5/2} - AEr^{III} \ ^4F_{7/2}} n_{Yb^{III} \ ^2F_{5/2}} n_{Er^{III} \ ^4I_{11/2}} - n \frac{Er^{III} \ ^4F_{7/2}}{\tau_{nr,Er^{III} \ ^4F_{7/2} \rightarrow Er^{III} \ ^2H_{11/2}}} \\
\frac{d n_{Er^{III} \ ^2H_{11/2}}}{dt} &= \frac{n_{Er^{III} \ ^4F_{7/2}}}{\tau_{nr,Er^{III} \ ^4F_{7/2} \rightarrow Er^{III} \ ^2H_{11/2}}} - \frac{n_{Er^{III} \ ^2H_{11/2}}}{\tau_{nr,Er^{III} \ ^2H_{11/2} \rightarrow Er^{III} \ ^4S_{3/2}}} - \frac{n_{Er^{III} \ ^2H_{11/2}}}{\tau_{r,Er^{III} \ ^2H_{11/2} \rightarrow Er^{III} \ ^4I_{15/2}}} \\
\frac{d n_{Er^{III} \ ^4S_{3/2}}}{dt} &= \frac{n_{Er^{III} \ ^4S_{3/2}}}{\tau_{nr,Er^{III} \ ^2H_{11/2} \rightarrow Er^{III} \ ^4S_{3/2}}} - \frac{n_{Er^{III} \ ^4S_{3/2}}}{\tau_{r,Er^{III} \ ^4S_{3/2} \rightarrow Er^{III} \ ^4I_{15/2}}} - \frac{n_{Er^{III} \ ^4S_{3/2}}}{\tau_{nr,Er^{III} \ ^4S_{3/2} \rightarrow Er^{III} \ ^4F_{9/2}}} \\
\frac{d n_{Er^{III} \ ^4F_{9/2}}}{dt} &= \frac{n_{Er^{III} \ ^4S_{3/2}}}{\tau_{nr,Er^{III} \ ^4S_{3/2} \rightarrow Er^{III} \ ^4F_{9/2}}} - \frac{n_{Er^{III} \ ^4F_{9/2}}}{\tau_{r,Er^{III} \ ^4F_{9/2} \rightarrow Er^{III} \ ^4I_{15/2}}} \\
&+ W_{DYb^{III} \ ^2F_{5/2} AEr^{III} \ ^4F_{9/2}} n_{Yb^{III} \ ^2F_{5/2}} n_{Er^{III} \ ^4I_{13/2}} - W_{DYb^{III} \ ^2F_{5/2} - AEr^{III} \ ^2H_{9/2}} n_{Yb^{III} \ ^2F_{5/2}} n_{Er^{III} \ ^4F_{9/2}} \\
\frac{d n_{Er^{III} \ ^4I_{11/2}}}{dt} &= - \frac{n_{Er^{III} \ ^4I_{11/2}}}{\tau_{nr,Er^{III} \ ^4I_{11/2} \rightarrow Er^{III} \ ^4I_{13/2}}} \\
&- W_{DYb^{III} \ ^2F_{5/2} AEr^{III} \ ^4F_{7/2}} n_{Yb^{III} \ ^2F_{5/2}} n_{Er^{III} \ ^4I_{11/2}} + W_{DYb^{III} \ ^2F_{5/2} AEr^{III} \ ^4I_{11/2}} n_{Yb^{III} \ ^2F_{5/2}} n_{Er^{III} \ ^4I_{15/2}}
\end{aligned}$$

$$I(t) = \sum_a f(t - aT); \quad f = I_0 e^{-\left(\frac{t-aT}{\tau}\right)^2}$$

PULSE PROPAGATION SIMULATIONS

$$\begin{aligned}
\frac{\partial H_y}{\partial t} &= -\frac{1}{\mu_0} \frac{\partial E_x}{\partial z}, \\
\frac{\partial E_x}{\partial t} &= -\frac{1}{\varepsilon} \frac{\partial H_y}{\partial z} - \frac{1}{\varepsilon} \frac{\partial P_x}{\partial t}
\end{aligned}$$

$$\frac{\partial}{\partial t}\begin{pmatrix}\rho_1\\ \rho_2\\ \rho_3\end{pmatrix}=\begin{pmatrix}0&\omega_0&0\\ \omega_0&0&2\frac{\mu}{\hbar}E_x\\ 0&2\frac{\mu}{\hbar}E_x&0\end{pmatrix}\begin{pmatrix}\rho_1\\ \rho_2\\ \rho_3\end{pmatrix}+\begin{pmatrix}\dot{g}(t)&0&0\\ 0&\dot{g}(t)&0\\ 0&0&\frac{1}{T_1}\end{pmatrix}\begin{pmatrix}\rho_1\\ \rho_2\\ \rho_3-\rho_{30}\end{pmatrix}$$